Bioactive Materials 9 (2022) 63–76

Contents lists available at ScienceDirect

Bioactive Materials

journal homepage: www.sciencedirect.com/journal/bioactive-materials

Near-infrared light triggered multi-hit therapeutic nanosystem for tumor specific photothermal effect amplified signal pathway regulation and ferroptosis

He Lian [a], Ping Guan [b], Hongyan Tan [c], Xiaoshu Zhang [c,*], Zhaoxu Meng [a,**]

[a] Department of Biomedical Engineering, School of Medical Instrumentation, Shenyang Pharmaceutical University, Shenyang, 110016, China
[b] School of Pharmacy, Shenyang Pharmaceutical University, Shenyang, 110016, China
[c] School of Functional Food and Wine, Shenyang Pharmaceutical University, Shenyang, 110016, China

ARTICLE INFO

Keywords:
Multi-hit therapy
HSP90
Ferroptosis
Photothermal effect

ABSTRACT

The high therapeutic resistance of tumor is the primary cause behind tumor recurrence and incurability. In recent years, scientists have devoted themselves to find a variety of treatments to solve this problem. Herein, we propose a multi-hit strategy that is based on the biodegradable hollow mesoporous Prussian blue (HMPB)-based nanosystem for tumor-specific therapy that encapsulated the critical heat shock protein 90 (HSP90) inhibitor 17-dimethylamino-ethylamino-17-demethoxydeldanamycin (17-DMAG). The nanosystem was further modified using thermotropic phase transition material star-PEG-PCL (sPP) and hyaluronic acid (HA), which offers near infrared light (NIR) responsive release characteristic, as well as enhanced tumor cell endocytosis. Upon cell internalization of 17-DMAG-HMPB@sPP@HA and under 808 nm laser irradiation, photothermal-conversion effect of HMPB directly kills cells using hyperthermia, which further causes phase transition of sPP to trigger release of 17-DMAG, inhibits HSP90 activity and blocks multiple signaling pathways, including cell cycle, Akt and HIF pathways. Additionally, the down-regulation of GPX4 protein expression by 17-DMAG and the release of ferric and ferrous ions from gradual degradation of HMPB in the endogenous mild acidic microenvironment in tumors promoted the occurrence of ferroptosis. Importantly, the antitumor effect of 17-DMAG and ferroptosis damage were amplified using photothermal effect of HMPB by accelerating release of ferric and ferrous ions, and reducing HSP90 expression in cells, which induced powerful antitumor effect *in vitro* and *in vivo*. This multi-hit therapeutic nanosystem helps provide a novel perspective for solving the predicament of cancer treatment, as well as a promising strategy for design of a novel cancer treatment nanoplatform.

1. Introduction

To date, a large number of anticancer drugs have been used clinically to treat variety of cancers. However, potential side effects caused by toxicity and occurrence of multi-drug resistance makes current treatment effect unsatisfactory [1–3]. Despite the fact that a wide range of inorganic and organic nanocarriers have emerged over recent years to alleviate the intractable problem, the potential toxicity [4,5], metabolic behavior and residual effects of these nanocarriers, especially non-biodegradable carriers, remain unknown, which brings new problems to cancer treatment [6,7]. This situation has led to a new high-efficiency and low-toxicity treatment model to become an inevitable trend.

With the development of biomedical nanotechnology, novel therapeutic techniques have been widely used in tumor treatment, including targeted chemotherapy, immunotherapy and phototherapy (PTT or PDT) [8–12]. However, the antitumor effects of these single treatment strategies have not been ideal. Therefore, we envision that if tumor-specific molecules can be loaded into safe and therapeutic carriers in order to achieve multi-hit therapy, that is, to block signal pathways from multiple points and destroy the entire signal pathway that cells depend on for survival, then it will be a beneficial method for improving efficacy. Importantly, this multi-hit therapy can effectively avoid problems of drug resistance caused by single-hit anticancer drugs,

Peer review under responsibility of KeAi Communications Co., Ltd.
* Corresponding author.
** Corresponding author.
E-mail addresses: xiaoshu2397@163.com (X. Zhang), 106040303@syphu.edu.cn (Z. Meng).

https://doi.org/10.1016/j.bioactmat.2021.07.014
Received 15 May 2021; Received in revised form 30 June 2021; Accepted 15 July 2021
Available online 21 July 2021

and will not reduce antitumor efficacy.

Recently, it has been shown that heat shock protein 90 (HSP90), a rich and highly conserved molecular chaperone, and its expression rate in tumor cells is two-to-ten times that of normal cells [13,14]. The downstream client protein of HSP90 contains numerous oncoproteins (rather than a single one), which are associated with multiple signal transduction proteins and have important roles in carcinogenic signal transduction, angiogenesis, metastasis, and anti-apoptosis [15]. Therefore, by inhibiting HSP90, and by inhibiting the downstream signal oncoprotein transduction, we are able to achieve a multi-point attack, interfere with tumor cell cycle, induce apoptosis, inhibit tumor invasion, and tumor metastasis [16,17]. This is where HSP90 inhibitors are more advantageous than other chemotherapy drugs.

HSP90 inhibitors compete with ATP in order to bind to the ATPase domain of HSP90 to inhibit the biological function of HSP90, which reduces the affinity of HSP90 to its client protein [18]. Compared to normal cells, HSP90 inhibitors have high specificity for cancer cells. In fact, it has been reported that the affinity of tumor-derived HSP90 and 17-allylamino-geldanamycin (17-AAG) is 100-times than that of normal tissues. Thus, HSP90 inhibitors can specifically kill tumors cells [19]. This makes HSP90 inhibitors an attractive new drug in the treatment of tumors over the past two decades. Compared to 17-AAG, the second-generation inhibitor, 17-dimethylamino-ethylamino-17-demethoxydeldanamycin (17-DMAG) has stronger water solubility, higher potency, less extensive metabolism and lower hepatotoxicity [20,21]. Studies have validated that 17-DMAG have exhibits encouraging results in melanoma, breast, ovarian, and prostate cancer cell lines, and has entered phase I clinical trials [22].

Prussian blue (PB) has been granted approval by the FDA as a clinical antidote for the treatment of thallium and cesium poisoning, which fully demonstrates its biological safety. In recent years, the application of PB has aroused great research interest, particularly in the field oncology, due to its excellent photothermal conversion performance [23,24]. In addition, hollow mesoporous PB nanoparticles (HMPB) were synthesized using controlled chemical etching. The huge hollow mesoporous structure inside makes it useful as a drug carrier [25,26]. In addition, ferric and ferrous ions, or other doped ions embedded on the surface of PB, can be released from the matrix under reactions of endogenous stimuli, including mild acidity, due to unstable Fe–C≡N–Fe bond under acidic conditions [27,28]. Therefore, we assume that HMPB can be a pH-responsive carrier for encapsulation of 17-DMAG, which triggers release of 17-DMAG, ferric and ferrous ions at the tumor site in order to achieve highly effective antitumor efficacy through synergistic multi-hit therapy, including photothermal effect/ferroptosis/cell signal transduction regulation. To the best of our best knowledge, a combination of ferroptosis based on Prussian blue and other treatment modalities have not yet been explored.

In detail, 17-DMAG was initially encapsulated into the inner cavity of HMPB. Next, in order to improve the responsive release behavior of the delivery system, the thermotropic phase transition material sPP was synthesized and then wrapped onto the surface of HMPB in order to achieve on-demand release under laser irradiation. The outer layer was coated with hyaluronic acid in order to improve the hydrophilicity and enhanced CD44 receptor-mediated endocytosis from tumor stroma into cells, which helps obtain the 17-DMAG-HMPB@sPP@HA delivery system. As presented in Scheme 1, after intratumoral injection, with the help of CD44-mediated endocytosis, the system accumulates within the cell and triggers release of 17-DMAG, ferric and ferrous ions under irradiation of near-infrared light and cellular acidic environment. Next, 17-DMAG down-regulates several carcinogenic pathways by inhibiting activity of HSP90, which includes cyclin A2, protein kinase Akt, p-Akt and hypoxia inducible factor HIF-1α. Next, accumulation of ferric and ferrous ions in cells and increasing reactive oxygen species leads to ferroptosis, which further inhibits proliferation of mouse melanoma B16 cells *in vivo* and *in vitro*. Importantly, in addition to the physical effects of hyperthermia to kill cells, the intrinsic photothermal capacity of 17-DMAG-HMPB@sPP@HA also augments the effects of the ferroptosis and signal pathway regulation due to increased release of ferric and ferrous ions and down-regulation of HSP90 expression, wherein complete elimination of tumors on B16 subcutaneous tumor-bearing mice has been achieved.

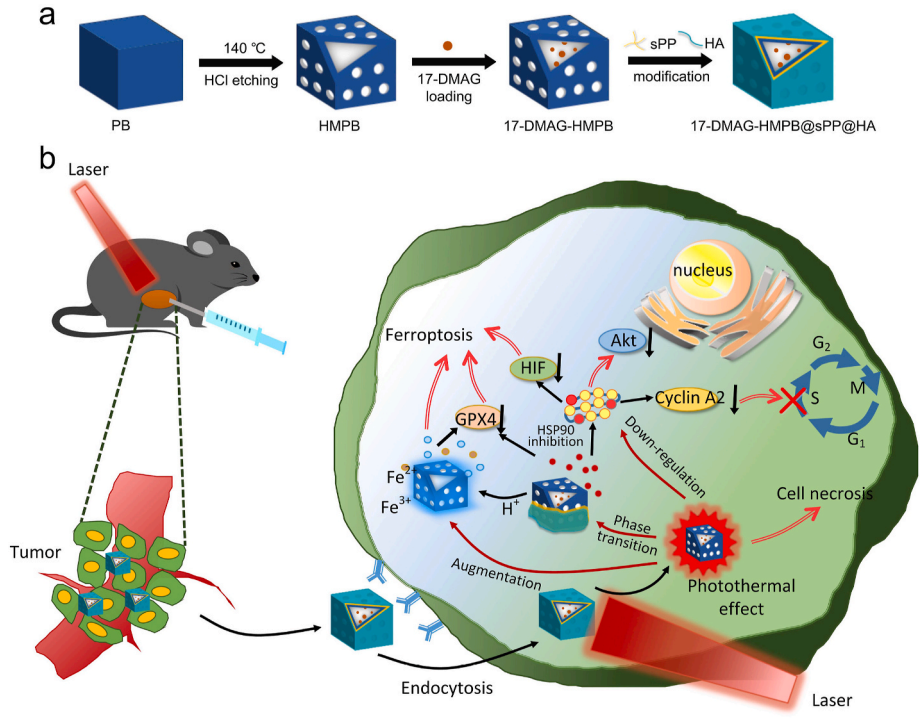

Scheme 1. (a) The construction process of 17-DMAG-HMPB@sPP@HA nanosystem. (b) Illustration the tumor specific multi-hit therapy including photothermal effect amplified signal pathway regulation and ferroptosis under NIR laser irradiation.

2. Materials and methods

2.1. Materials

Four-armed polyethylene glycol 2000 Da (star-PEG) was purchased from Qiyue Biotechnology Co., Ltd (Xi'an, China). CL monomers, Sn $(Oct)_2$, alvespimycin (17-DMAG) HCl, poly (vinyl pyrrolidone) (PVP, K30), potassium hexacyanoferrate (III) (K_3 $[Fe(CN)_6]$), and hyaluronic acid (HA, 20 KDa) were bought from Macklin Co. (Shanghai, China). Fetal bovine serum (FBS), RPMI 1640 medium, cell counting kit-8 (CCK-8), calcein AM/PI cell viability assay kit, annexin V-FITC apoptosis detection kit, cell cycle and apoptosis analysis kit and DCFH-DA were also acquired from Meilun Biotechnology Co. (Dalian, China). The cyclin A2 rabbit monoclonal antibody, Akt, phospho-Akt (Ser 473), HSP90-1α, HSP70 and GPX4 rabbit polyclonal antibody were purchased from the Beyotime Biotechnology Co. (Haimen, China). ACSL4 mouse monoclonal antibody were bought from Sigma-Aldrich Co. (USA).

2.2. Synthesis characterization of sPP copolymer

The synthesis of sPP copolymer was carried out according to a previous report [29] with some minor changes. In brief, a 4.4 mmol star-PEG was dissolved in 180 mL of toluene and the solution was heated to 120 °C in order to remove the water. Then, the appropriate amount of CL monomers and $Sn(Oct)_2$ catalyst (0.02:1, mol/mol) were added. After refluxing for 12 h, the solvent was then extracted and the product was precipitated using cold diethyl ether. The chemical structure and molecular weight were evaluated by the ^1H NMR spectra and gel permeation chromatography, the melting behavior was analyzed using differential scanning calorimetry (DSC) (Mettler Toledo DSC-1, Switzerland).

2.3. Preparation and characterization of PB, HMPB and 17-DMAG-HMPB@sPP@HA nanoparticles (NPs)

For preparation of PB NPs, 3 g of PVP was dissolved into 40 mL of HCl solution (0.01 mol L^{-1}), after which 132 mg K_3 $[Fe(CN)_6]$ was added and stirred for 30 min. The mixture solution was then transferred to a preheated oven at 80 °C for 24 h. Then, the synthetic PB NPs were gathered by centrifugation (11 000 rpm, 10 min) and washed three times using deionized water. In order to prepare HMPB NPs, 10 mg PB and 100 mg PVP were dissolved in 10 mL HCl solution (1 mol L^{-1}) and stirred for 3 h. Next, the mixture solution was transferred into a Teflon-sealed autoclave and heated for 3 h at 140 °C. After centrifugation and washing with deionized water three times, the HMPB NPs were obtained.

The drug loading process was carried out by equilibrium adsorption method. Briefly, HMPB NPs was dispersed in the ethanol solution, stirred overnight and washed twice in order to remove excess PVP from the surface. Then, the 17-DMAG (5 mg) was dissolved in water and added to the HMPB solutions (1 mg mL^{-1}). After that, the mixed solution was stirred for 3 h for 17-DMAG loading, then the 17-DMAG-HMPB NPs were gathered using centrifugation (13 000, 5 rpm). The sPP copolymer was dissolved into hexafluoroisopropanol (HFIP) (10 mg mL^{-1}), and the 17-DMAG-HMPB NPs were added into it and stirred for 90 min, so that the sPP material was able to seal the pores on the particle surface, because its hydrophobic PCL segment entered into the interior of HMPB NPs due to the hydrophobic force, leaving the star-PEG segment outside the nanoparticle. After centrifugation, 17-DMAG-HMPB@sPP NPs were added into the mixed solvent (HFIP: water, 2:1, v/v) that contained HA and was stirred for an additional 90 min. In this way, HA was wrapped in the outermost part of the particles through hydrogen bonding and molecular entanglement with PVP and star-PEG. Then, the 17-DMAG-HMPB@sPP@HA NPs were gathered using centrifugation and washing.

The morphology and structure of samples were measured using transmission electron microscopy (TEM) (Tecnai G20, FEI, USA). The hydrodynamic diameters and zeta potentials were identified using the Malvern Zetasizer Nano series (Malvern, UK). The absorption curves were examined via the uv–vis spectrophotometer (UV–1800PC). Then, the thermogravimetric analysis was conducted on thermogravimetric analyzer (TGA-2, Mettler Toledo).

2.4. Release of 17-DMAG from 17-DMAG-HMPB@sPP@HA NPs

The 17-DMAG-HMPB@sPP@HA NPs were sealed in a dialysis bag (Mw = 3500 Da) and dispersed into a PBS solution (pH = 6.5) with continuous stirring at 37 °C. At different intervals, a dialysis bag was irradiated under laser for 5 min (1 W cm^{-2}). Then, the cumulative release was calculated by quantifying absorption value of the release medium at various time points.

2.5. Photothermal performance of HMPB@sPP@HA NPs

The HMPB@sPP@HA solutions (40, 80, 160 μg mL^{-1}, 1 mL) were placed into a glass tube and exposed to an 808 nm laser (1 W cm^{-2}, Ningbo Yuanming Laser Technology Co., Ltd, China). In addition, the 17-DMAG-HMPB@sPP@HA solution (80 μg mL^{-1}, 1 mL) was irradiated at different power densities (1, 1.5, 2 W cm^{-2}). Temperature changes and infrared images were gathered using a photothermal imager (FLIR, USA). Then, the absorption curve and particle size prior to and after irradiation were also examined.

2.6. Cell culture

The mouse melanoma cell line (B16) was purchased through the Cell Bank of the Chinese Academy of Sciences (Shanghai, China). B16 cells were maintained in an RPMI 1640 medium supplemented with 10% FBS and 1% antibiotics were cultured into a 5% CO_2 incubator at 37 °C.

2.7. In vitro antitumor activity

The B16 cells were seeded into 96-well plate (3×10^4 cells per well) and incubated for 24 h. Then, the cells were exposed to 17-DMAG and 17-DMAG-HMPB@sPP@HA with an equivalent of 17-DMAG (0, 3, 6, 9, 12 and 15 μg mL^{-1}), while the other groups were dosed with similar concentrations of HMPB (0, 6.25, 12.5, 25, 50 and 100 μg mL^{-1}). Furthermore, the untreated cells were utilized as controls. The cell-level photothermal effects of HMPB@sPP@HA and 17-DMAG-HMPB@sPP@HA were also evaluated. In brief, after incubating with HMPB@sPP@HA or 17-DMAG-HMPB@sPP@HA for 12 h, cells were irradiated under an 808 nm laser for 5 min (1.5 W cm^{-2}) and then incubated for another 12 h. The standard CCK-8 assay was utilized for measurement of cell viabilities.

2.8. In vitro CLSM observation

B16 cells were seeded into a 6-well plate with coverslips and incubated for 24 h. Then, the cells were incubated with 17-DMAG (15 μg mL^{-1}), HMPB@sPP, HMPB@sPP@HA, or 17-DMAG@sPP @HA (100 μg mL^{-1}) for another 24 h. In order to observe the photothermal antitumor effect, cells were initially incubated with either HMPB@sPP@HA or 17-DMAG-HMPB@sPP@HA for 12 h, exposed to the 808 nm laser for 5 min (1.5 W cm^{-2}) and finally incubated for an additional 12 h. After, cells were stained using the calcein AM/PI cell viability assay kit and observed under a CLSM microscope (Zeiss, Germany).

2.9. Flow cytometry analysis

For flow cytometry analysis, B16 cells were seeded onto 6-well plates (1×10^5 cells per well) and treated with 17-DMAG (7.5 μg mL^{-1}), HMPB@sPP@HA, HMPB@sPP@HA + Laser (1.5 W cm^{-2}, 5 min), or 17-DMAG-HMPB@sPP@HA + Laser (1.5 W cm^{-2}, 5 min) (100 μg mL^{-1}), as

described above. Prior to apoptosis analysis, cells were collected, washed with PBS and re-suspended within the binding buffer (100 μL). FITC (5 μL) and PI (10 μL) were added into he buffer in order to stain cells in dark for 30 min. For cell cycle analysis, the treated cells were collected, washed with PBS and fixed in ethanol for at least 2 h. Then, the cells were treated with PI staining solution containing PI and RNase A in the dark for 30 min. For ROS level analysis, treated cells were incubated with DCFH-DA (10 μM) for 25 min, and washed with PBS twice. All samples were tested through a FACS flow cytometer.

2.10. Western blot analysis

Western blotting was utilized to detect protein expression. After extraction, the protein content in cell or tumor lysate was determined by the BCA protein quantitative kit. Subsequently, proteins were resolved using an SDS-polyacrylamide gel electrophoresis, transferred to a nitrocellulose membrane and sealed with 5% skim milk. After incubation with primary and secondary antibodies, the enhanced chemiluminescence method was utilized to display the bands. After exposure, the bands were observed and analyzed using the GraphPad Prism software.

2.11. Animal experiments

All animal protocols were granted approval by the Animal Research Committee of the Shenyang Pharmaceutical University. The C57BL/6 and Kunming mice (6–8 weeks) were purchased from Changsheng biotechnology Co. Ltd (Benxi, China).

2.12. In vivo antitumor efficiency evaluation

The subcutaneous xenograft B16 tumor model was established in the C57BL/6 mice. The mice were randomly divided into six groups (n = 5), and the B16 cells (2×10^6) were injected into the right armpit. When the tumor volume reached 100 mm^3, the mice were treated with either saline (control group), laser (808 nm, 1 W cm^{-2}), 17-DMAG (1.5 mg kg^{-1}), HMPB@sPP@HA (10 mg kg^{-1}), HMPB@sPP@HA (10 mg kg^{-1}) + laser (808 nm, 1 W cm^{-2}), or 17-DMAG-HMPB@ sPP@HA (10 mg kg^{-1}) + laser (808 nm, 1 W cm^{-2}), respectively. The drug was intratumorally injected once a week and laser irradiation was carried out 4 h after injection. The body weight and tumor volume were quantified every two days after administration. At the end of treatment, the mice were euthanized, and tumors were harvested for TUNEL, H&E, Ki-67, HSP90 immunohistochemical staining and Western blot assays.

2.13. In vivo distribution

The healthy Kunming mice were randomly divided into six groups (n = 3), and were injected subcutaneously with 17-DMAG-HMPB@ sPP@HA (10 mg kg^{-1}). At different time intervals, the injection site and *ex-vivo* major organs (heart, liver, spleen, lungs and kidney) were exposed under laser irradiation for 5 min (808 nm, 1 W cm^{-2}), temperature changes and infrared images were gathered using a photothermal imager (FLIR, USA).

2.14. In vivo biocompatibility assay

The *in vivo* biocompatibility of 17-DMAG-HMPB@sPP@HA system was carried out on healthy Kunming mice. The mice were divided into four groups randomly (n = 5) and subcutaneously injected with saline, 17-DMAG (5 mg kg^{-1}), HMPB@sPP@HA and 17-DMAG-HMPB@sPP@HA (20 mg kg^{-1}), respectively. After 14 days, the blood samples were collected for further testing. The harvested organs were fixed in 4% paraformaldehyde, sliced into 5 μm sections, and stained using hematoxylin and eosin (H&E) for microscopy observation.

2.15. Statistical analysis

All values are presented as mean ± standard deviations (SD). Statistical analysis was carried out using the Student's *t*-test for two groups, as well as one-way analysis of variance for more than two groups. $*p < 0.05$ and $**p < 0.01$ were considered to be significant and highly significant differences, respectively.

3. Results and discussion

3.1. Characterization of sPP copolymer and 17-DMAG-HMPB@sPP@HA NPs

The thermotropic phase transition material sPP copolymer, which consisted of star-PEG2000 and terminal PCL1000 segment, was successfully synthesized (Fig. 1a). The obtained copolymer was a kind of white waxy solid (Fig. 1b), the structure of which was further characterized using ^{1}H NMR (Fig. S1). The proton peaks at δ 2.6 and δ 3.6 corresponded to the methylene protons of CL and PEG, respectively. In the IR spectra (Fig. 1c), the stretching vibration peak of $\nu_{C=O}$ appeared at 1724 cm^{-1}, while the asymmetric stretching vibration (ν_{as} C–O–C), symmetric stretching vibration (ν_s C–O–C) and the deformation vibration (δ C–O–C) emerged at 1245 cm^{-1}, 1107 cm^{-1}, and 961 cm^{-1}, respectively, which suggests the formation of an ester bond between star-PEG and PCL. The relative molecular weight of sPP copolymer (Mw) obtained by GPC method was 7125 Da (Fig. S2), and the polydispersity index was 1.609 (Tab. S1). The melting range of sPP copolymer reflected by the DSC analysis ranged from 36.4 °C to 59.3 °C (Fig. 1d). This means that at room temperature, sPP copolymer is in a rubbery state, and after reaching the melting point as the temperature rises, it changes from the rubbery state to a viscous flow state. Since the star copolymer has a lower melting point than linear copolymers of homologous composition and molecular weight, the obtained sPP copolymer is a promising material for the antitumor application of photothermal-induced phase transition on-demand drug delivery system.

The HMPB NPs were prepared using the "two-step" method, as illustrated in scheme 1a. The monodispersed PB nanoparticles were initially formed by oriented aggregating. Next, the hollow structure was obtained through further chemical etching by HCl at 140 °C, under the protection of PVP. Next, the NIR responsiveness of the prepared HMPB NPs was investigated. The absorption value indicated a good linear relationship, with a concentration in the range of 5–60 μg mL^{-1} (R^2 = 0.9993, Fig. 1h and i), indicating that HMPB can be utilized as a promising photothermal converter. Next, HMPB NPs were washed with ethanol and water in order to remove the PVP from the surface for improved loading of 17-DMAG. after that, the particles were covered using the phase transition material sPP by stirring due to the hydrophobic force between the PCL segment of sPP copolymer and the interior of HMPB. Finally, HA was utilized to coat on the outer surface because of hydrogen bonding and its molecular entanglement with PVP and star-PEG, in order to increase hydrophilicity and enhanced cellular endocytosis as the CD44 receptor is overexpressed across a variety of cancer cells.

The morphology of obtained PB, HMPB and 17-DMAG-HMPB@sPP@HA were characterized using transmission electron microscopy (Fig. 1e–g). The images demonstrated that these particles were monodispersed (110 nm). Furthermore, the PBs with cubic structure became smooth and hollow after etching, and the particle size increased slightly after loading of 17-DMAG and modification reflected by the hydrated particle size, as analyzed with DLS (Fig. 1k). Zeta potentials demonstrated that PB and HMPB particles were negatively charged (Fig. 1l), but the value increased to −5.35 mv after drug loading and modification due to surface covering of sPP copolymer. On the contrary, the zeta potential decreased to −34.44 mv after HA coating, which validated the formation of 17-DMAG-HMPB@sPP@HA. Using the UV-NIR scanning spectrums (Fig. 1j), we did not find obvious absorption

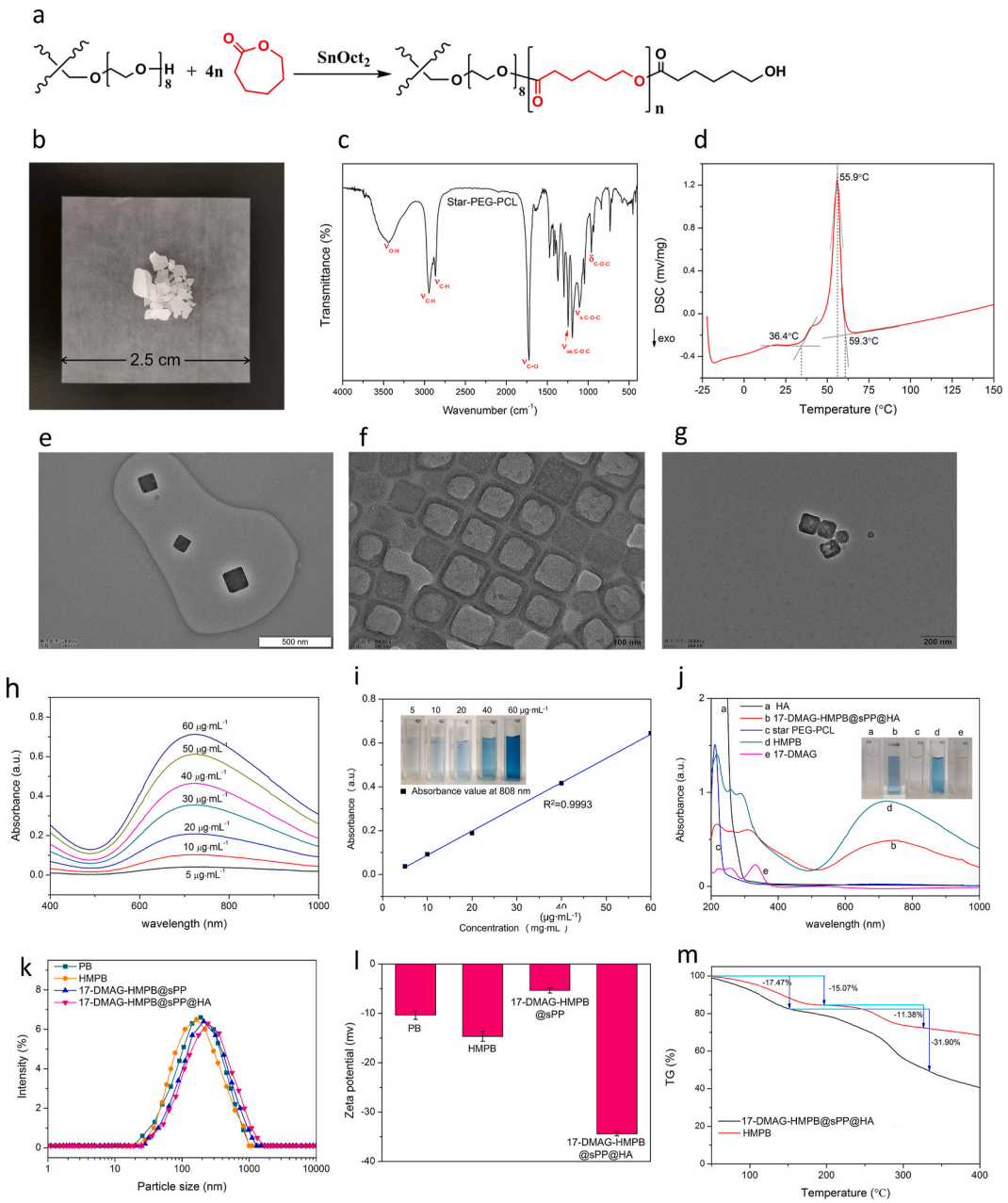

Fig. 1. The (a) synthesis process (a), appearance (b), and IR spectra (c) of the sPP copolymer. (d) Melting point of the sPP copolymer, as reflected by the DSC curve. (e–g) TEM images of PB, HMPB and 17-DMAG-HMPB@sPP@HA. (h) The Vis-NIR absorbance spectrums of HMPB solutions at different concentrations ranging between 400 and 1000 nm. (i) The standard curve of maximum absorption value to HMPB concentration. (j) The UV-NIR absorbance spectra and optical appearance of 17-DMAG, sPP copolymer, HA, HMPB and 17-DMAG-HMPB@sPP@HA. The particle size distribution (k) and zeta potentials (l) by DLS analysis. (m) The thermal gravimetric curves of HMPB and 17-DMAG-HMPB@sPP@HA.

peaks in the curves of sPP copolymer and HA. However, HMPB demonstrated a broad absorption peak that ranged from 650 to 850 nm, which covers the NIR-1 region (808 nm), as well as the 17-DMAG aqueous solution prior to being loaded into the HMPB, which has a maximum absorption peak at 331 nm. This peak also existed in the absorption curve of 17-DMAG-HMPB@sPP@HA with a little blue shift, which indicates the interaction between 17-DMAG and interior of HMPB. Besides, after calculation, the maximum loading efficiency of 17-DMAG was 13.23%. Furthermore, 17-DMAG-HMPB@sPP@HA has a similar characteristic peak as HMPB, demonstrating that it can also be used as PTT agent. In the TG curve for HMPB (Fig. 1m), the weight losses were 15.07% and 11.38% at 0–20 °C and 200–330 °C, respectively. However, the 17-DMAG-HMPB@sPP@HA curve demonstrated more significant losses of 17.47% and 31.90% at 0–150°Cand 150–340 °C, respectively, which was attributed to decomposition of 17-DMAG, sPP copolymer and HA, and further confirmed the existence of 17-DMAG-HMPB@sPP@HA nanosystem.

The realization of tumor treatment by inhibiting heat shock protein (HSP90) and regulating the cell signaling pathway largely depends on the effective on-demand release of 17-DMAG from the prepared 17-DMAG-HMPB@sPP@HA. Therefore, we investigated the release of 17-DMAG in pH 6.5 buffer solution in order to simulate biomimetic tumor microenvironment (Fig. S3). The results revealed that the release of 17-DMAG was obviously NIR-light dependent, particularly, under the intermittent 808 nm laser irradiation. Furthermore, 17-DMAG-HMPB@sPP@HA demonstrated a corresponding burst release pattern

due to melting of the phase transition material sPP caused by photothermal effect and stripping from HMPB particle surface. In addition, the accumulative release percentage was 62.41% when incubating for 24 h. In comparison, 17-DMAG-HMPB@sPP@HA demonstrated a considerable physicochemical stability without laser irradiation, whereas the total 17-DMAG release percentage was only 17.35%, which indicated that 17-DMAG-HMPB@sPP@HA can effectively achieve a goal of on-demand drug release.

3.2. Photothermal-conversion performance of HMPB@sPP@HA

Firstly, HMPB@sPP@HA solutions at different concentrations were exposed to the 808 nm laser irradiation (1 W cm^{-2}, Fig. 2a). The temperature of the solution with a relatively low concentration (40 μg mL^{-1}) was elevated up to 51.5 °C, while the temperature of the solution with the highest concentration (160 μg mL^{-1}) was able to reach 64.9 °C. Comparatively, there was no obvious temperature change of control group under the same condition. Furthermore, we investigated the temperature change of the solution (80 μg mL^{-1}) under different laser irradiation intensities (Fig. 2d). The temperature increased with an augment of laser intensity, and was able to reach to 76.3 °C under laser irradiation at 2 W cm^{-2}. This demonstrated that HMPB@sPP@HA possesses an excellent photothermal-conversion performance, and can be utilized as a photothermal agent to increase the antitumor effect of 17-DMAG. Photothermal images that correspond to the heating curves are shown Fig. 2d and e. In order to further explore the photothermal stability of HMPB@sPP@HA, the temperature changes across four cycles of heating to the highest temperature and then cooling to 37 °C by laser-on/off rounds were recorded. We observed no significant attenuation of photothermal performance, suggesting that HMPB@sPP@HA is able to generate effective and durable heat under NIR irradiation (Fig. 2c). According to heat transfer time constant and difference between the maximum temperature and minimum temperature, the photothermal conversion efficiency (η) at 808 nm is calculated, which is as high as 47.21% (Fig. 2f). We measured the absorption curve and particle size prior to and after laser irradiation, and discovered no significant change, which further validated the photostability of HMPB@sPP@HA (Fig. 2g and h).

3.3. In vitro antitumor activity

In vitro antitumor activity of various treatments on B16 cells were investigated using the cell counting kit-8 (CCK-8) assays. Compared to the group with only laser irradiation, the HMPB@sPP@HA + Laser

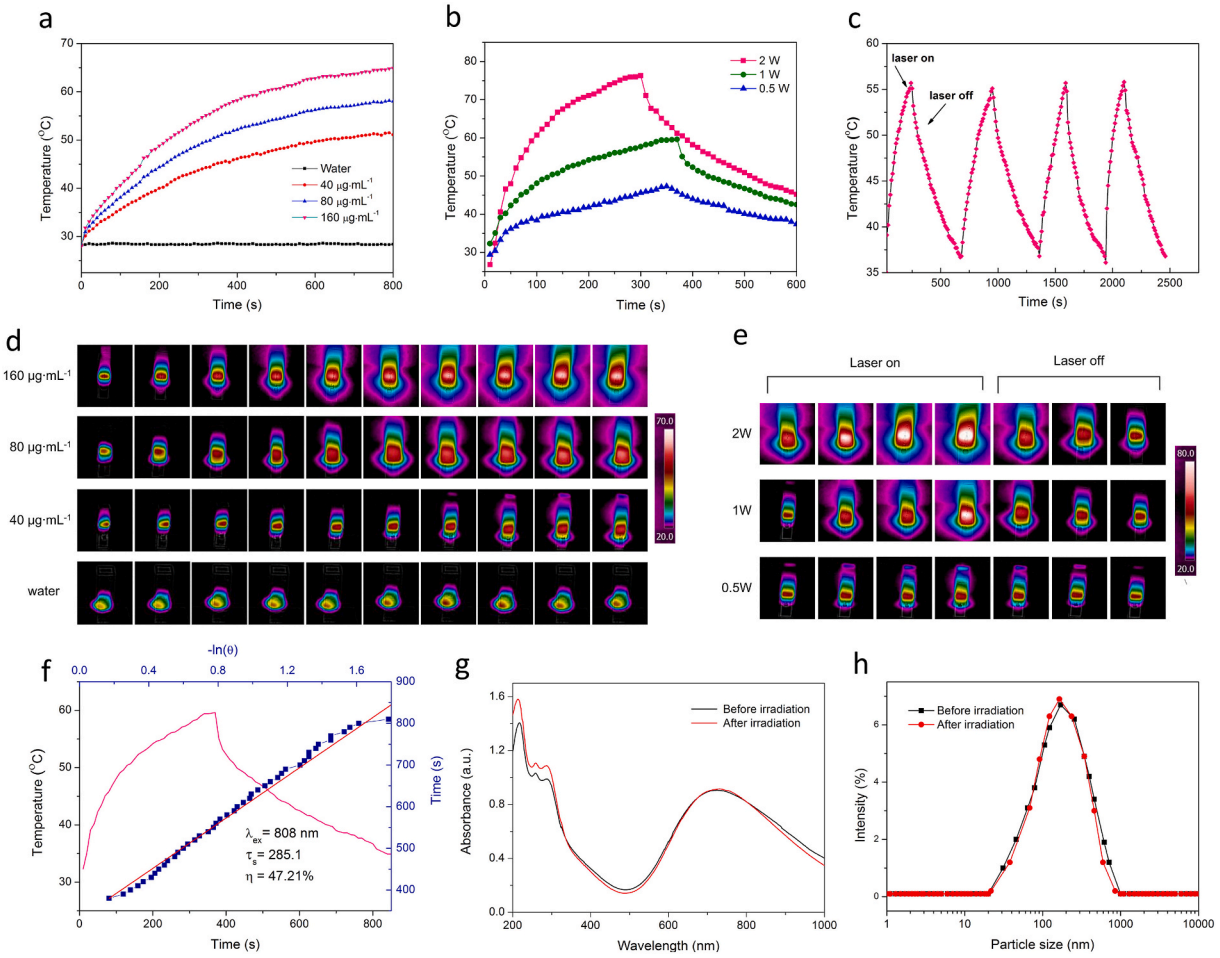

Fig. 2. (a) The photothermal-conversion performance of HMPB@sPP@HA at different concentrations (40, 80 160 μg mL^{-1}) under the 808 nm laser irradiation (1 W cm^{-2}). (b) Heating and cooling curves of HMPB@sPP@HA under the 808 nm laser on/off irradiation at different intensities (0.5, 1 and 2 W cm^{-2}). (c) The photothermal-conversion performance of HMPB@sPP@HA over four laser-on/off rounds (1 W cm^{-2}). (d) The photothermal images under continuous laser irradiation, corresponding to Fig. 2a. (e) The photothermal images under laser on/off irradiation, corresponding to Fig. 2b. (f) Photothermal-conversion efficiency of HMPB@sPP@HA at 808 nm. The pink line represents temperature change curves of the solution under 808 nm laser on/off irradiation at 2 W cm^{-2}. The blue line represents heat transfer time constant (τ_s), obtained by regression analysis of the linear time date from the cooling curve. (g) The UV-NIR spectrums of HMPB@sPP@HA solution before and after four laser on/off irradiation rounds. (h) The particle size of HMPB@sPP@HA before and after four laser on/off irradiation rounds.

group exerted a significant influence on cell viability, which indicated the excellent photothermal therapy performance (Fig. 3a). Interestingly, the cell viabilities also gradually decreased at both the elevated concentration of HMPB@sPP and HMPB@sPP@HA without laser irradiation (Fig. 3b), which suggests some potential cytotoxic mechanisms need to be further explored. As there is no obvious change in cell viability in the groups sPP copolymer and HA (Fig. S4), and there was a large amount of iron in the structure of PB (Fe_4 $[Fe(CN)_6]_3$), we speculated whether ferroptosis occurs in this part of the cell. Additionally, the cytotoxicity of HMPB@sPP@HA was stronger compared to HMPB@sPP due to enhanced endocytosis by binding of HA with the CD44 receptor on the cell surface. In addition, free 17-DAMG and 17-DMAG-HMPB@sPP@HA at equal concentration of 17-DMAG exerted effective antitumor activity, while the latter was stronger (Fig. 3c). Importantly, the 17-DMAG-HMPB@sPP@HA had the strongest cell-killing effect upon NIR laser irradiation (Fig. 3d). Even at a relatively low concentration (6.25 μg mL^{-1}), the cell viability decreased to 48.94%, and with an elevation of concentration, the viability decreased to the lowest, at 3.91%. This indicated a more powerful therapeutic efficacy of synergistic 17-DMAG-HMPB@sPP@HA. The corresponding highest cell death rate in each group and the calculated IC_{50} values are shown in Fig. 3e and f.

Moreover, calcein-AM and PI were utilized to stain the living and dead cells for visualization under CLSM. We observed bright green fluorescence signals in the control and laser groups, revealing no damage in the cells. In contrast, the red PI signals began to appear in the group that was incubated with HMPB@sPP and HMPB@sPP@HA, the green and red signals could be observed at the same time, which suggests some damage to the cells that may be caused by ferroptosis. Furthermore, bright red fluorescence were observed in 17-DMAG, 17-DMAG-

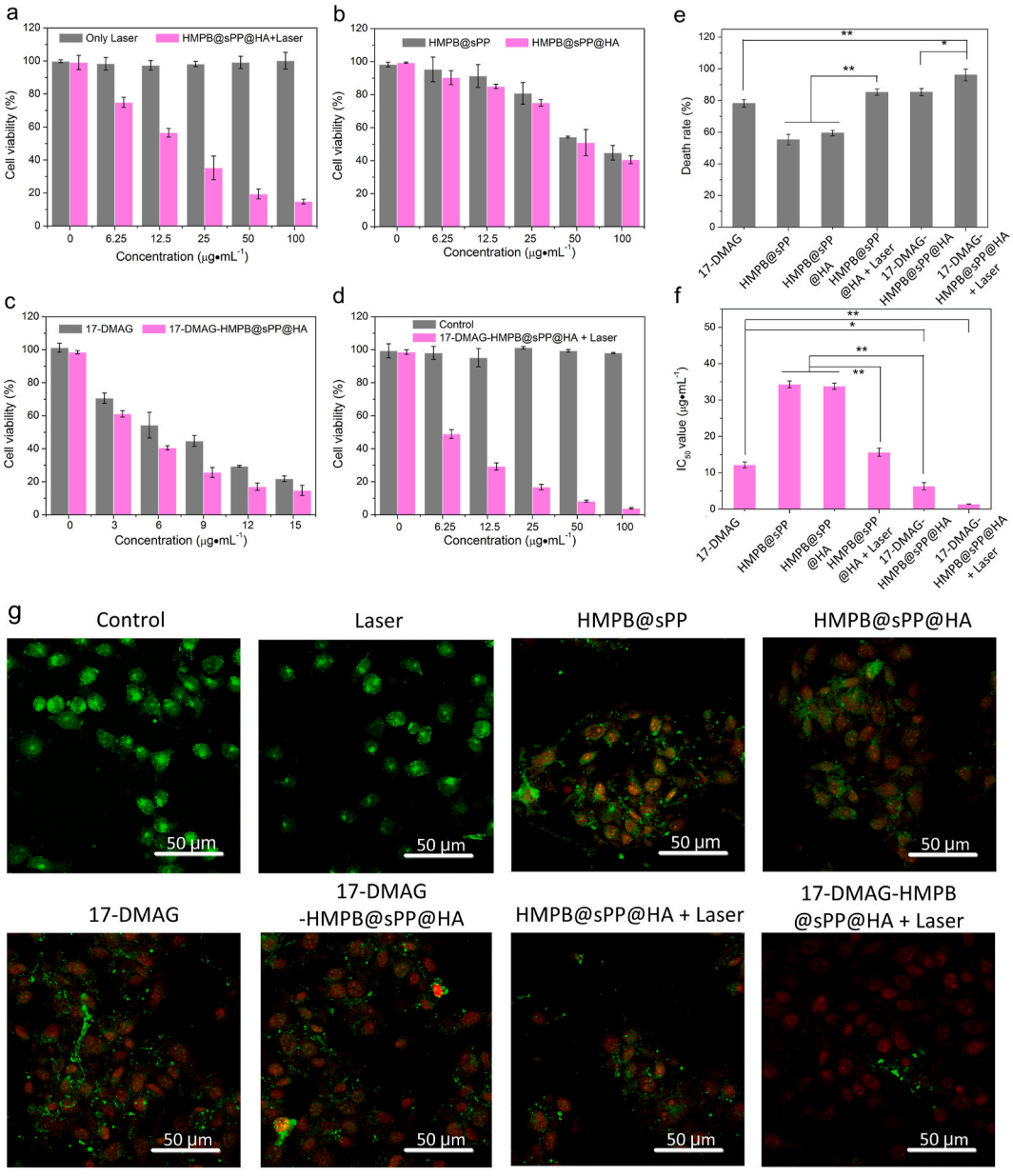

Fig. 3. *In vitro* cytotoxicity profiles. (a–d) The relative cell viabilities of B16 cells across the different treatment groups, including negative control, laser, HMPB@sPP@HA + laser at different concentrations, HMPB@sPP and HMPB@sPP@HA and 17-DMAG-HMPB@sPP@HA + laser at different concentrations, 17-DMAG and 17-DMAG-HMPB@sPP@HA at equivalent 17-DMAG concentrations. (e) The cell death rate at the highest concentration in each group. (f) The IC_{50} value for each group. (g) The CLSM images of B16 cells across the treatment groups stained by calcein-AM (for living cells) and PI (for dead cells), respectively. The laser irradiation intensity was 1.5 W cm^{-2}, and the irradiation duration was 5 min.

HMPB@sPP@HA and HMPB@sPP@HA + laser group, and green fluorescence became scattered in dots, which indicates the presence of more obvious cytotoxicity, and the cell membrane began to break. The strongest red signals were observed in the 17-DMAG-HMPB@sPP@HA + laser group, which demonstrates much more effective lethality performance on B16 cells.

3.4. Investigation into the therapeutic mechanism of 17-DMAG-HMPB@sPP@HA nanosystem in vitro

We sought to explore the cell death mechanisms behind the 17-DMAG-HMPB@sPP@HA therapeutic system using various complementary techniques. Initially, the cell death pathways were analyzed using flow cytometry through FITC-labeled Annexin V and PI in order to stain the live and dead B16 cells (Fig. 4a). Consistent with results from the CCK-8 assay, it was indicated that a combination treatment of 17-DMAG-HMPB@sPP@HA + Laser group demonstrated the best synergistic therapeutic efficacy and total ratio of dead/late apoptotic cells was as high as 51.7%, which was higher than that induced by the monotherapies of 17-DMAG (23.8%) and HMPB@sPP@HA + Laser (31.6%) (Fig. 4b). Besides, the B16 cells incubated with HMPB@sPP@HA were also induced to undergo late-stage apoptosis and necrosis, which further confirmed the previous inference that HMPB@sPP@HA causes cell death, probably ferroptosis. It is noteworthy that after cells were incubated with various treatment groups, the living cells, late apoptotic cells and dead cells were all observed, with the exception of early apoptotic cells, which indicates that 17-DMAG-HMPB@sPP@HA + Laser treatment does not induce cell death through the apoptotic pathway. Necrotic cells emerged due to extreme physical and chemical changes that was brought by the photothermal effect, which is consistent earlier reports in literature [30].

Next, in order to further investigate the cellular inhibitory mechanism, cell cycle distribution of B16 cells treated with various groups were evaluated using flow cytometry after staining with PI. The results indicated that after 17-DMAG and 17-DMAG-HMPB@sPP@HA + Laser treatment, the proportion of B16 cells in the S phase significantly increased (Fig. 4c and d), while cell cycle distribution changed little after HMPB@sPP@HA and HMPB@sPP@HA + Laser treatment, which suggested that 17-DMAG is able to block cells in the S phase and inhibit their proliferation.

Importantly, since 17-DMAG is an effective heat shock protein inhibitor, we investigated how the 17-DMAG-HMPB@sPP@HA treatment system affects HSP90, as well as the downstream multiple signaling pathways. Western blot results demonstrated that 17-DMAG does not affect the expression of HSP90 and homotype protein HSP70 (Fig. 4e), which is consistent with literature that reports that 17-DMAG competes with ATP in order to bind to the N-terminal region of HSP90, and thus changes the activity of HSP90. In contrast, the photothermal effect caused an observable decrease in expression of HSP90.

Additionally, 17-DMAG down-regulated the expression of cyclin A2, which is able to decrease its binding with the cyclin kinase, CDK2, leading to failure of E2F transcription factor inactivation and cellular transition from S phase to G2 phase [31,32]. This was consistent with previous result of the S phase block by 17-DMAG. The regulation of multiple signaling pathways in cells by 17-DMAG-HMPB@sPP@HA + Laser treatment system was also reflected in the decreased expression of protein kinase B (Akt), phosphorylated protein kinase B (p-Akt) and hypoxia inducible factor (HIF-1α). Activated Akt has an anti-apoptotic role by phosphorylating the target protein via multiple downstream pathways, such as stimulating glucose metabolism and regulating cell cycle, inhibiting activity of proteolytic enzyme caspase-9, preventing activation of apoptosis cascade, and phosphorylating p53 binding protein, MDM2, to regulate the activity of p53 [33,34]. Additionally, HIF-1α, as an important transcription factor of cancer cells under hypoxic conditions, regulates angiogenesis, glucose metabolism, apoptosis and autophagy, and participates in regulating multiple signaling pathways, and then regulates processes of cell growth, proliferation, migration and apoptosis [35,36]. Thus, the inhibition of these signaling pathways is of great significance, which indicates that melanoma can be treated through this mechanism.

In addition to the mechanisms outlined above, we further examined the occurrence of ferroptosis induced by HMPB, as we observed cell death in HMPB@sPP@HA in the CCK-8 assay and Annexin V-FITC/PI staining cell apoptosis experiment *in vitro*. Ferroptosis is a kind of necrotic cell death catalyzed by iron ions. It is characterized by the inactivation of the intracellular reducing system and the destruction of lipid molecules containing long chains of unsaturated fatty acids on cell membrane or organelle membrane by peroxidation, resulting in the rupture of cell membrane. This form of cell death was named ferroptosis by Stockwell in 2012 [37]. The increase in iron accumulation, the production of oxidative free radicals, and lipid peroxidation are the key factors of ferroptosis [38]. Thus, we initially examined ROS levels in B16 cells after different treatments. It is discovered that ROS levels reflected by DCF intensity in HMPB@sPP@HA, HMPB@sPP@HA + Laser, and 17-DMAG-HMPB@sPP@HA + Laser groups were 1.59, 2.04 and 2.87-fold higher, respectively, compared to the control group (Fig. 5a and b). Meanwhile, we observed that intracellular iron levels were increased by 16.21, 18.98 and 23.88-fold, respectively (Fig. 5c), which immediately suggests that HMPB in the nanosystem substantially induced ferroptosis in B16 cells.

Moreover, we observed that the cellular ROS levels after laser irradiation were higher compared to without laser, which is likely due to the photothermal effect, as it accelerates the dissociation of ferric and ferrous ions from HMPB in cells. Furthermore, the 17-DMAG-HMPB@sPP@HA + Laser group has the highest ROS level, suggesting the dual role of 17-DMAG as heat shock protein inhibitor and ferroptosis enhancer. It has been reported that HIF-1α is able to increase the expression of fatty acid binding protein (FABP3 and FABP7), which could promote fatty acid intake, improve lipid storage capacity, and subsequently avoid lipid peroxidation in order to resist ferroptosis [38]. Alternatively, sensitivity of cells to ferroptosis was enhanced by 17-DMAG, HMPB@sPP and 17-DMAG-HMPB@sPP@HA by inhibiting expression of HIF-1α. It has also been reported that 17-DMAG can promote ferroptosis in gastric cancer cells by changing the balance of oxidants and antioxidants, leading to increased ROS levels and reduced expression of glutathione peroxidase (GPX4) [39]. The Western blot results offered a more pronounced evidence to the results above and validated that the decreased expression of GPX4, which accelerates the peroxidation on membrane lipids (Fig. 5d). Herein, we concluded that the 17-DMAG-HMPB@sPP@HA treatment system in this study exerts an excellent antitumor effect via multi-hit complementary roles, which includes photothermal effect, cell signaling pathway regulation and ferroptosis.

3.5. In vivo evaluation on the antitumor efficacy

After validating the multiple synergistic antitumor mechanisms of 17-DMAG-HMPB@sPP@HA nanosystem on tumor cells, we further investigated the *in vivo* antitumor efficacy of this system on B16 tumor-bearing mice. The establishment and treatment of B16 subcutaneous tumor models are described in Fig. 6a. In brief, C57BL/6 mice with B16 xenograft tumors were randomly divided into six groups and treated with PBS, laser, 17-DMAG, HMPB@sPP@HA, HMPB@sPP@HA + laser, and 17-DMAG-HMPB@sPP@HA + laser, respectively. We ensured that an equivalent amount of 17-DMAG existed in the solution alone, as well as in the DMAG-loaded nanosystem. The body weights and tumor volumes were recorded every other day during treatment.

The photothermal therapeutic performance of 17-DMAG-HMPB@sPP@HA *in vivo* was initially estimated. The 808 nm laser was irradiated on the tumor of II, Vand VI groups in 4 h after intratumoral injection. In the case of laser irradiation only, the temperature at the tumor site demonstrated a slow upward trend due to melanin in the

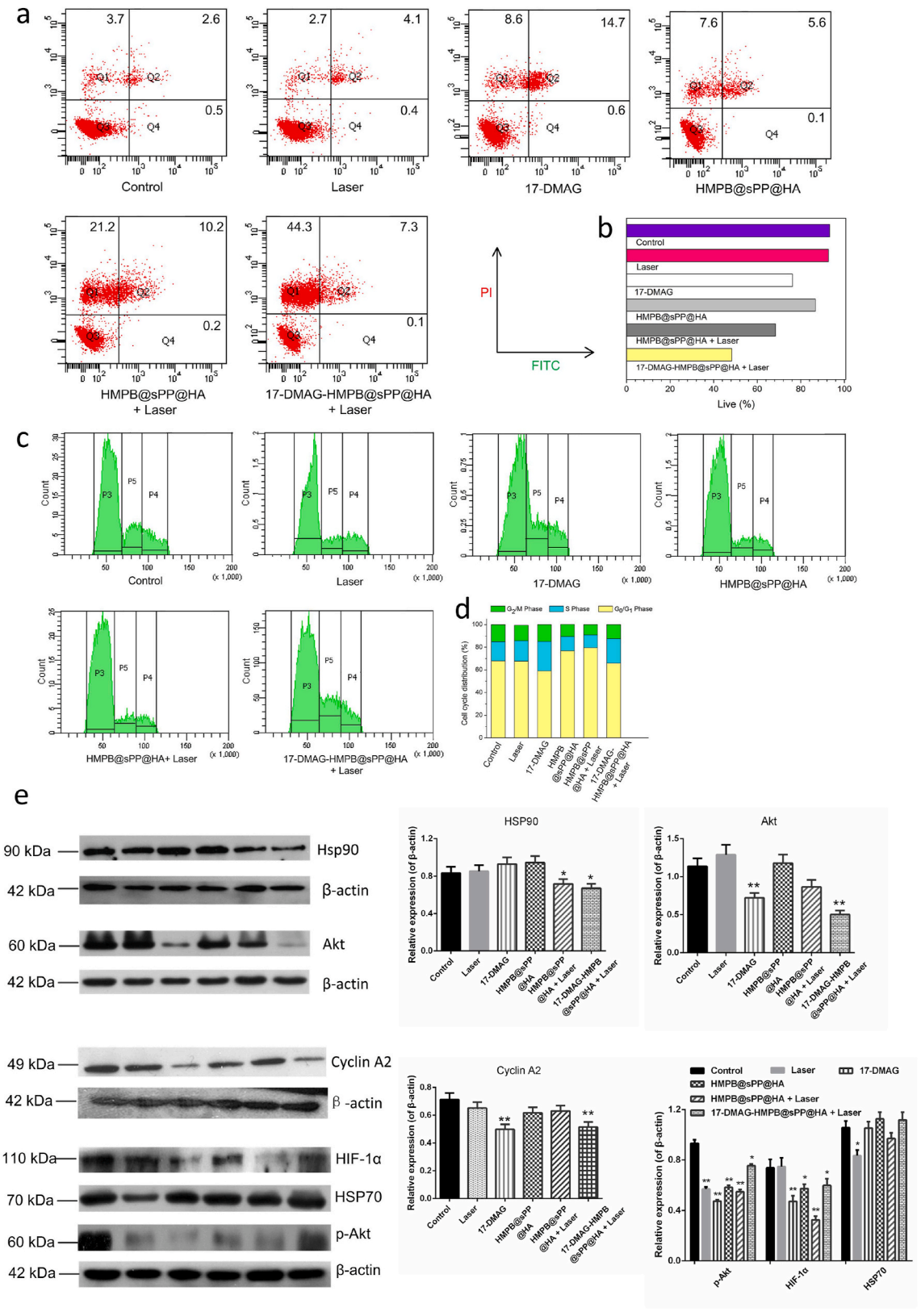

Fig. 4. (a) Flow cytometry analysis of apoptosis stage on B16 cells after different treatments. (b) The quantitative results of cell death percentage, including late apoptosis cells and dead cells. (c) The cell cycle distribution of B16 cells after different treatments. (d) The quantitative analysis of cell cycle distribution. (e) Western blot assays for protein expression in the B16 cells after different treatments and the grayscale analysis results of the protein bands, compared to the corresponding β-actin protein. (n = 3, $^{*}P < 0.05$, $^{**}P < 0.01$).

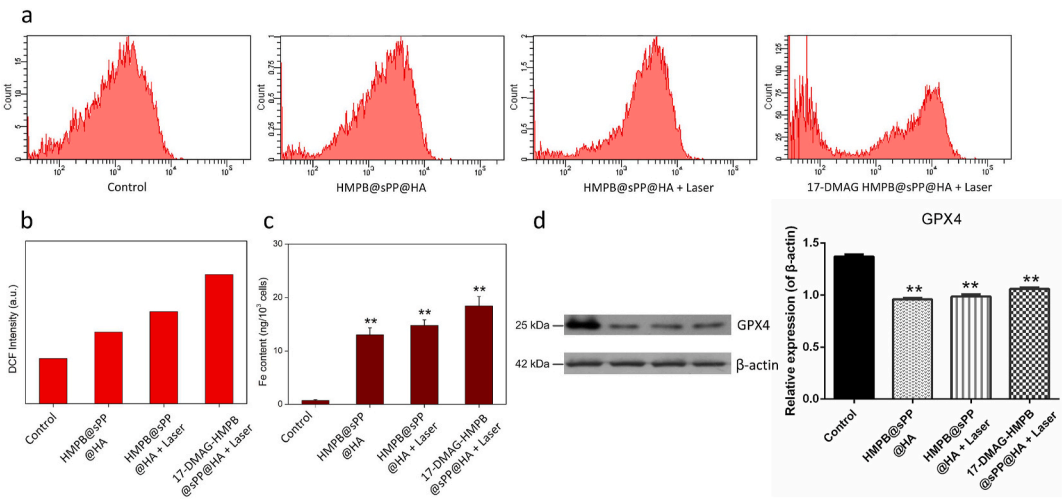

Fig. 5. Analysis of ferroptosis on B16 cells. (a) Reactive oxygen species (ROS) in B16 cells after different treatments. (b) The histogram analysis of ROS content is reflected by DCF fluorescence. (c) The Fe content in B16 cells after different treatments. (d) The Western blot assays for GPX4 level in B16 cells after different treatments and the grayscale analysis result, compared to β-actin protein. (n = 3, $^{**}P < 0.01$).

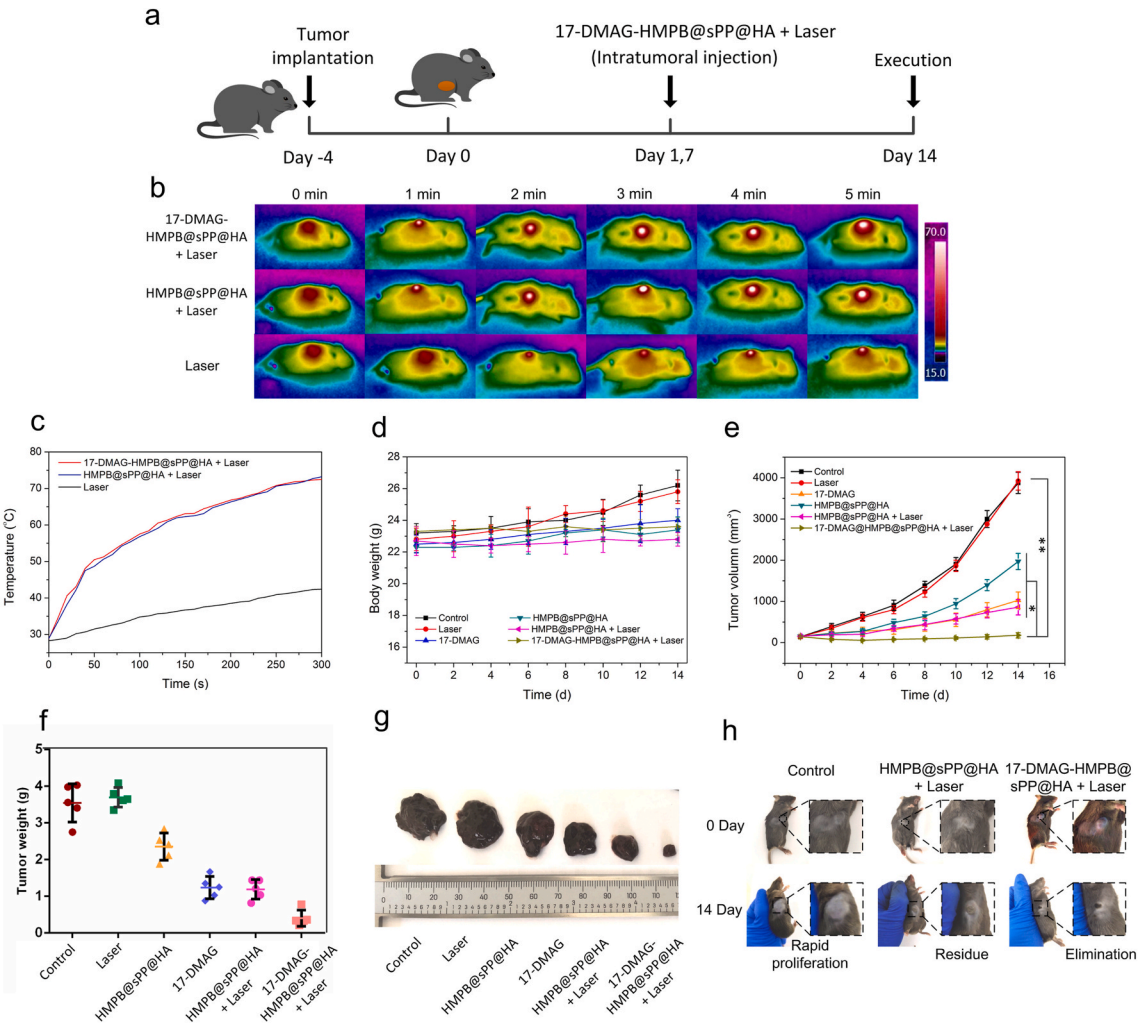

Fig. 6. *In vivo* antitumor efficacy of 17-DMAG-HMPB@sPP@HA on B16 xenograft tumor bearing mice. (a) Schematic diagram of the tumor model establishment and treatment of 17-DMAG-HMPB@sPP@HA on the B16 xenograft tumor bearing mice. (b) Photothermal images of mice under an 808 nm laser irradiation after different treatments. (c) Temperature change curves at the subcutaneous tumor site under laser irradiation. The body weight changes (d), tumor volume changes (e) and the final tumor weights (f) of C57BL/6 mice after different treatments. (g) Images of final tumor tissues collected from tumor-bearing mice. (h) Images of mice after the various treatments, wherein tumor growths were compared to the beginning of treatment. (n = 5, mean ± SD, $^{*}p < 0.05$, $^{**}p < 0.01$).

melanoma cells. However, the overall change was not significant. In comparison, for the Vand VI groups, temperature at the tumor site increased rapidly to 72.3 °C, which is definitely an effective tumor-killing temperature (Fig. 6b and c), demonstrating the excellent photothermal-conversion efficiency of 17-DMAG-HMPB@sPP@HA *in vivo*.

During the two weeks' treatment, the body weights of mice in the control and laser groups increased to a certain extent due to the rapid growth and large volume of tumors (Fig. 6d), which was approximately 4000 mm^3 (Fig. 6e), while the tumor weights were 3.55 and 3.69 g, respectively (Fig. 6f). In comparison, growth of subcutaneous tumors in the III, IV, and Vgroups were significantly suppressed, which was reflected by suppressed tumor growth curves and tumor weights, and confirmed the effectiveness of 17-DMAG, HMPB and the photothermal effect. Encouragingly, the most pronounced tumor inhibition effect was found in the 17-DMAG-HMPB@sPP@HA + Laser group, where tumor size was significantly reduced, and a part of tumors were eliminated without reoccurrence during the whole treatment period. This effect was

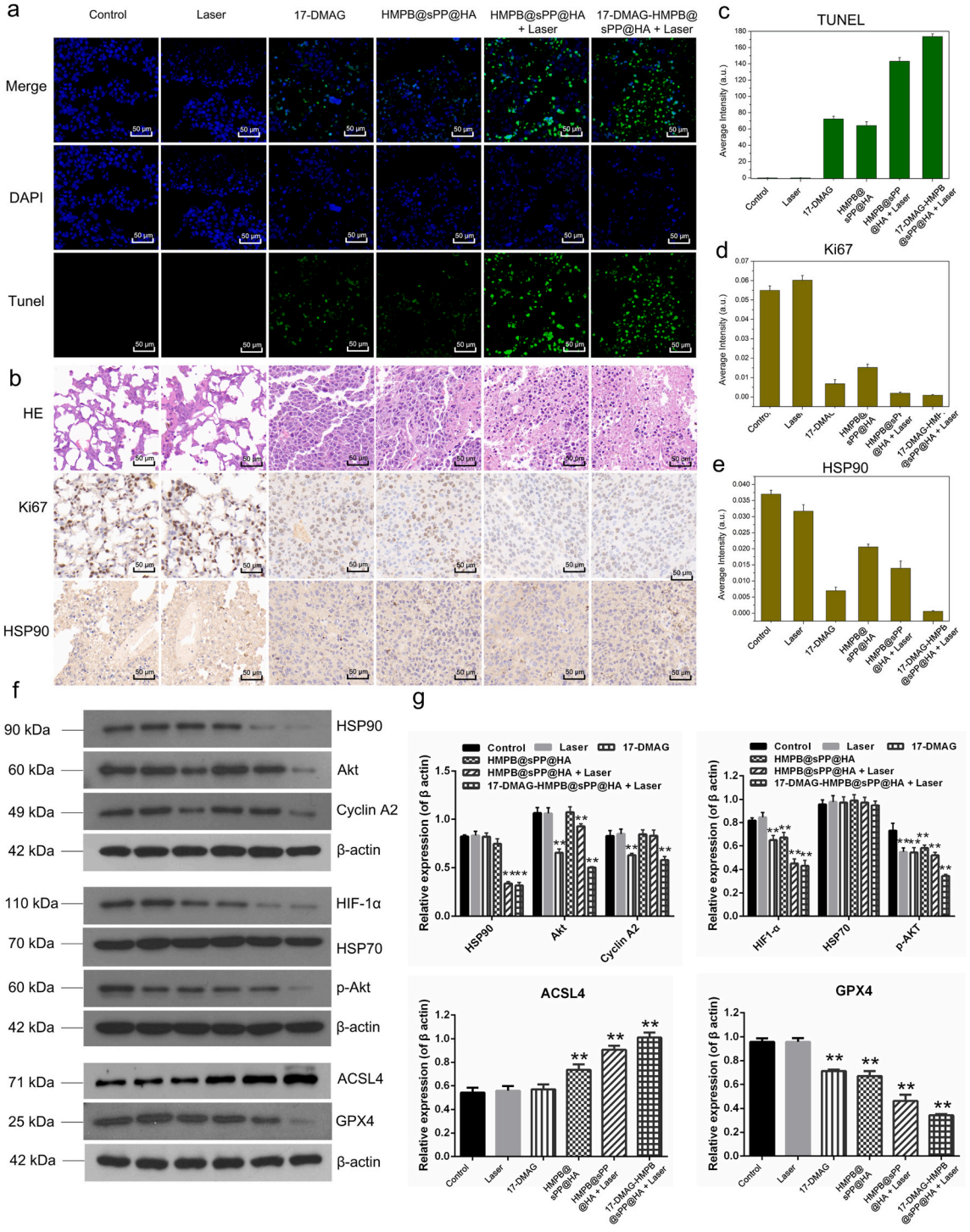

Fig. 7. (a) The TUNEL assay. (b) HE, Ki67 and HSP90 antigen immunohistochemistry-stained sections of B16 tumors, and (c–e) the corresponding positive expression calculated by the ImagePro Plus software (Mean ± SD, n = 3). (f) Western blot assays for protein expression in tumors after different treatments and (g) the grayscale analysis results of the protein bands, compared to the corresponding β-actin protein. (n = 3, $^{*}P < 0.05$, $^{**}P < 0.01$).

reflected by the photos of the tumors under the skin and after dissection (Fig. 6g and h). Moreover, mice in the valid treatment groups all survived till the end of treatment, while mice in the control and laser groups had a certain mortality rate, and two and one mice died in each group, respectively, due to the large size and deep invasion of the tumor. Furthermore, terminal deoxynucleotidyl transferase dUTP nick end labeling (TUNEL) staining (Fig. 7a) hematoxylin and eosin (H&E), Ki-67, and HSP90 immunohistochemical staining (Fig. 7b) were carried out on tumor pathological sections, which further confirmed the most effective tumor inhibition of 17-DMAG-HMPB@sPP@HA through complementary multi-hit therapy. The corresponding quantitative results obtained by ImagePro Plus software were shown in Fig. 7c, d and 7e.

The expression and regulation of signal pathways and ferroptosis related proteins in tumors were monitored using Western blot assays (Fig. 7f). The results are consistent with the results from the *in vitro* therapeutic mechanism investigation. Our data demonstrate that 17-DMAG-HMPB@sPP@HA nanosystem suppressed multiple signaling pathway proteins, such as Akt, p-Akt, HIF and cyclin A2, through HSP90 inhibition by 17-DMAG and down-regulated HSP90 expression by photothermal effect. The nanosystem also induced ferroptosis in tumors, which was reflected in the up-regulation of GPX4 and down-regulation of long-chain acyl-CoA synthetases 4 (ACSL4) by the accelerated iron release by photothermal effect. 17-DMAG also contributed to ferroptosis by down-regulation of GPX4 which changing the redox homeostasis in tumor. The gray-scale analysis and significance test results are shown in Fig. 7g.

The *in vivo* distribution of 17-DMAG-HMPB@sPP@HA nanosystem was also evaluated. However, HMPB nanoparticles have a broad and strong absorption peak in the range of 600–850 nm, which covers the excitation wavelength of most NIR responsive dyes, such as the frequently used fluorescent dye DiR at 748 nm. The DiR loaded HMPB@sPP@HA nanoparticles we prepared can not be excited to emit fluorescence to be examined by *in vivo* near-infrared fluorescence imaging technology, due to the strong photothermal conversion of HMPB from NIR excitation light into heat energy. Alternatively, we performed near-infrared photothermal imaging on the subcutaneous injection site after laser irradiation to analyze the distribution of particles *in vivo*, and the *ex-vivo* images of major organs (heart, liver, spleen, lungs and kidney) under laser irradiation at different time points after injection were also provided (Fig. S7). The results showed that 17-DMAG-HMPB@sPP@HA nanosystem could stay at the injection site stably after subcutaneous injection, and showed excellent photothermal effect under laser irradiation. The average temperature of the injection site could rise to more than 70 °C within 12 h, and slightly decreased at 24 h, but the average temperature was still 69.2 °C. Correspondingly, the distribution of 17-DMAG-HMPB@sPP@HA nanosystem to the major organs (heart, liver, spleen, lungs and kidney) was less. Compared with the control group, there was no significant change in the temperature.

In addition to the antitumor efficacy evaluations above, we investigated the biocompatibility of 17-DMAG-HMPB@sPP@HA on healthy Kunming mice in order to guarantee the safety for clinical application in the future. Kunming mice were randomly divided into four groups and then subcutaneously injected with PBS, 17-DMAG, HMPB@sPP@HA and 17-DMAG-HMPB@sPP@HA. The body weights of these mice were recorded every two days, and their blood indexes were assessed at the end of the evaluations. During the entire two-week observation period, we observed no significant body weight loss in each group, and all the mice were alive (Fig. S5a and b). Similarly, with regards to blood analysis, there were no significant parameter fluctuations observed in the cardiac, hepatic and renal function makers, as well as blood indexes, which suggests a negligible toxicity in mice (Fig. S5c-i). In order to gain more intuitive evidence of the biocompatibility of 17-DMAG-HMPB@sPP@HA, the main organs (heart, liver, spleen, lung, kidney) of mice were collected and stained using hematoxylin and eosin (H&E) for histological analysis. The results demonstrated no apparent pathological changes in the main organs (Fig. S6). All the results mentioned above demonstrated good biocompatibility of 17-DMAG-HMPB@sPP@HA nanosystem.

Traditional chemotherapy drugs have limited therapeutic effects due to their non-tumor-specific distribution *in vivo*, which is a major challenge for cancer treatment [40,41]. In contrast, photothermal therapy, especially near-infrared II (NIR-II) light-responsive nano-formulations with high photothermal stability and high photostability, can be used for the treatment of malignant tumors [42]. For example, Bian et al. reported a new type of NIR-II absorbing organic semiconductor amphiphilic polymer (OSPA) to enhance the stability and luminescence properties of organic semi-solid conductive polymer nanoparticles (OSPN) [43]. The maximum absorption wavelength of OSPA nanoparticles is located at 1000 nm, which enables the nanoparticles to achieve the photothermal treatment of subcutaneous and brain tumors under the guidance of photoacoustic imaging.

In the past decade, the rapid development of targeted delivery systems uses specific ligands in the drug delivery system to bind to specific receptors on the surface of tumor cells, such as folic acid and hyaluronic acid, which greatly improves the efficiency of drug delivery [44,45]. However, in the concept of cancer precision medicine, the ideal carrier can deliver personalized drugs to specific tumor tissues in specific patients. Since even the same cancer expresses different levels of cell surface receptors in different patients, targeted drug delivery is not effective in solving this problem. In recent years, newly emerged peptide-homing technology can improve the efficiency of drug delivery, prolong the half-life of drugs and avoid the side effects of off-target [46]. In particular, Mao et al. reported that the tumor-homing peptide guided targeting system based on phage display technology are able to quickly and economically select homing peptides, which have a clear targeting effect on unknown types of tumors without needing to know the target before [47]. This system demonstrated convincing precision treatment in the MCF-7 breast cancer-bearing mice, and it was completed in the same laboratory using the same animal model. Therefore, it is reasonable to believe that the combination of tumor-homing technology with NIR-II light responsive photothermal therapy and multi-hit therapy will make great strides forward in the precise treatment of tumor.

4. Conclusion

Herein, we constructed a multi-hit therapeutic NIR light-triggered release nanosystem by encapsulating 17-DMAG into hollow mesoporous Prussian blue nanostructures and functionalized the surface through the use of the thermotropic phase transitions material sPP, as well as the hydrophilic and cell surface binding material hyaluronic acid. After injection and distributed to the entire tumor site, the triggered release of 17-DMAG enabled by the photothermal effect under laser irradiation led to significant changes across multiple signaling transduction pathways in tumor cells by inhibiting heat shock protein HSP90, which resulted in an effective antitumor effect. Furthermore, mild acidic environment in tumor cells enabled degradation of HMPB, as well as the cytosolic release of Fe^{3+} and Fe^{2+}, which induced the production of ROS and lipid oxidation, causing cells to suffer ferroptotic damage. Importantly, based on the intrinsic photothermal conversion feature of HMPB, the antitumor efficacy was found to be greatly improved, and the therapeutic effects of 17-DMAG and ferroptosis were additionally augmented by the photothermal effect, and eventually achieved powerful tumor growth inhibition. Both the systematic *in vitro and in vivo* experiments suggested that the constructed synergistic 17-DMAG-HMPB@sPP@HA nanosystem was able to break through the dilemma of traditional treatment methods and offer a promising strategy for effective tumor therapies.

CRediT authorship contribution statement

He Lian: Methodology, Data curation, Conceptualization, Writing – original draft. **Ping Guan:** Data curation, Software. **Hongyan Tan:**

Validation, Formal analysis. **Xiaoshu Zhang:** Conceptualization, Data curation, Visualization. **Zhaoxu Meng:** Supervision, Writing – review & editing, Funding acquisition.

Declaration of competing interest

The authors declare that they have no known competing financial interests or personal relationships that could have appeared to influence the work reported in this paper.

Acknowledgments

This work was supported by: National Natural Science Foundation of China (Grant No: 81503020), Natural Science Foundation of Liaoning Province (Grant No: 2019-ZD-0459, 2020-MS-196), and the Basic Research Project of Liaoning Provincial Department of Education (Grant No: 2019LJC04).

Appendix A. Supplementary data

Supplementary data related to this article can be found at https://doi.org/10.1016/j.bioactmat.2021.07.014.

References

[1] N. Vasan, J. Baselga, D.M. Hyman, A view on drug resistance in cancer, Nature 575 (2019) 299–309, https://doi.org/10.1038/s41586-019-1730-1.
[2] J. Shi, P.W. Kantoff, R. Wooster, O.C. Farokhzad, Caner nanomedicine: progress, challenges and opportunities, Nat. Rev. Canc. 17 (2017) 20–37, https://doi.org/10.1038/nrc.2016.108.
[3] N. Chatterjee, T.G. Bivona, Polytherapy and targeted cancer drug resistance, Trends Cancer 5 (2019) 170–182, https://doi.org/10.1016/j.trecan.2019.02.003.
[4] M.J. Mitchell, M.M. Billingsley, R.M. Haley, M.E. Wechsler, N.A. Peppas, R. Langer, Engineering precision nanoparticles for drug delivery, Nat. Rev. Drug Discov. 20 (2021) 101–124, https://doi.org/10.1038/s41573-020-0090-8.
[5] S. Manchun, C.R. Dass, P. Sriamornsak, Targeted therapy for cancer using pH-responsive nanocarrier systems, Life Sci. 90 (2012) 381–387, https://doi.org/10.1016/j.lfs.2012.01.008.
[6] A. Wicki, D. Witzigmann, V. Balasubramanian, J. Huwyler, Nanomedicine in cancer therapy: challenges, opportunities, and clinical applications, J. Contr. Release 28 (2015) 138–157, https://doi.org/10.1016/j.jconrel.2014.12.030.
[7] J.I. Hare, T. Lammers, M.B. Ashford, S. Puri, G. Storm, S.T. Barry, Challenges and strategies in anti-cancer nanomedicine development: an industry perspective, Adv. Drug Deliv. Rev. 108 (2017) 25–38, https://doi.org/10.1016/j.addr.2016.04.025.
[8] S. Qin, A. Zhang, X. Zhang, Recent advances in targeted tumor chemotherapy based on smart nanomedicines, Small 14 (2018), e1802417, https://doi.org/10.1002/smll.201802417.
[9] R.S. Riley, C.H. June, R. Langer, M.J. Mitchell, Drug technologies for cancer immunotherapy, Nat. Rev. Drug Discov. 18 (2019) 175–196, https://doi.org/10.1038/s41573-018-0006-z.
[10] X. Zhang, J. Tang, C. Li, Y. Lu, L. Cheng, J. Liu, A targeted black phosphate nanoparticles based immune cells nano-regulator for photodynamic/photothermal and photoimmunotherapy, Bioact. Mater. 6 (2020) 472–489, https://doi.org/10.1016/j.bioactmat.2020.08.024.
[11] M. Lan, S. Zhao, W. Liu, C. Lee, W. Zhang, P. Wang, Photosensitizers for photodynamic therapy, Adv. Healthc. Mater. 8 (2019), e1900132, https://doi.org/10.1002/adhm.201900132.
[12] Z. Yu, W. Chan, Y. Zhang, T. Tan, Neat-infrared-IIactivated inorganic photothermal nanomedicines, Biomaterials 269 (2021) 120459, https://doi.org/10.1016/j.biomaterials.2020.120459.
[13] E. Pick, Y. Kluger, J.M. Giltnane, C. Moeder, R.L. Camp, D.L. Rimm, H.M. Kluger, High HSP90 expression is associated with decreased survival in breast cancer, Canc. Res. 67 (2007) 2932–2937, https://doi.org/10.1158/0008-5472.CAN-06-4511.
[14] C.H. Song, S.Y. Park, K. Eom, J.H. Kim, S. Kim, J.S. Kim, I.A. Kim, Potential prognostic value of heat-shock protein 90 in the presence of phophatidylinositol-3-kinase overexpression or loss of PTEN, in invasive breast cancers, Breast Cancer Res. 12 (2010) R20, https://doi.org/10.1186/bcr2557.
[15] P. Workman, F. Burrows, L. Neckers, N. Rosen, Drugging the cancer chaperone HSP90: combinatorial therapeutic exploitation of oncogene addiction and tumor stress, Ann. N. Y. Acad. Sci. 1113 (2007) 202–216, https://doi.org/10.1196/annals.1391.012.
[16] S.A. Lang, D. Klein, C. Moser, A. Gaumann, G. Glockzin, M.H. Dahlke, W. Dietmaier, U. Bolder, H.J. Schlitt, E.K. Geissler, O. Stoeltzing, Inhibition of heat shock protein 90 impairs epidermal growth factor-mediated signaling in gastric cancer cells and reduces tumor growth and vascularization in vivo, Mol. Canc. Therapeut. 6 (2007) 1123–1132, https://doi.org/10.1158/1535-7163.MCT-06-0628.
[17] F. Burrows, H. Zhang, A. Kamal, HSP90 activation and cell cycle regulation, Cell Cycle 12 (2004) 1530–1536, https://doi.org/10.4161/cc.3.12.1277.
[18] C.E. Stebbins, A.A. Russo, C. Schneider, N. Rosen, F.U. Hartl, N.P. Pavletich, Crystal structure of an HSP90-geldanamycin complex: targeting of a protein chaperone by an antitumor agent, Cell 89 (1997) 239–250, https://doi.org/10.1016/s0092-8674(00)80203-2.
[19] F. Paduano, R. Villa, M. Pennati, M. Folini, M. Binda, M.G. Daidone, N. Zaffaroni, Silencing of survivin gene by small interfering RNAs produces supra-additive growth suppression in combination with 17-allylamino-17-demethoxygeldanamycin in human prostate cancer cell, Mol. Canc. Therapeut. 5 (2006) 179–186, https://doi.org/10.1158/1535-7163.MCT-05-0132.
[20] S. Tsutsumi, L. Neckers, Extracellular heat shock protein 90: a role for a molecular chaperone in cell motility and cancer metastasis, Canc. Sci. 98 (2007) 1536–1539, https://doi.org/10.1111/j.1349-7006.2007.00561.x.
[21] J.L. Eiseman, J. Lan, T.F. Lagattuta, D.R. Hamburger, E. Joseph, J.M. Covey, M. J. Egorin, Pharmacokinetics and pharmacodymamics of 17-demethoxy 17-[[2-dimethylamino)ethyl]amino]geldanamycin (17DMAG, NSC 707545) in C.B-17 SCID mice bearing MDA-MB-231 human breast cancer xenografts, Cancer Chemother, Pharma 55 (2005) 21–32, https://doi.org/10.1007/s00280-004-0865-3.
[22] K. Jhaveri, K. Miller, L. Rosen, B. Schneider, L. Chap, A. Hannah, Z. Zhong, W. Ma, C. Hudis, S. Modi, A phase-Idose-escalation trial of trastuzumab and alvespimycin hydrochloride (KOS-1022; 17 DMAG) in the treatment of advanced solid tumors, Clin. Canc. Res. 18 (2012) 5090–5098, https://doi.org/10.1158/1078-0432.CCR-11-3200.
[23] L. Jing, X. Liang, Z. Deng, S. Feng, X. Li, M. Huang, C. Li, Z. Dai, Prussian blue coated gold nanoparticles for simultaneous photoacoustic/CT bimodal imaging and photothernal ablation of cancer, Biomaterials 35 (2014) 5814–5821, https://doi.org/10.1016/j.biomaterials.2014.04.005.
[24] Z.G. Qin, Y. Li, N. Gu, Progress in applications of Prussian blue nanoparticles in biomedicine, Adv. Healthc. Mater. 7 (2018), e1800347, https://doi.org/10.1002/adhm.201800347.
[25] R. Yang, M. Hou, Y. Gao, L. Zhang, Z. Xu, Y. Kang, P. Xue, Indocyanine gree-modified hollow mesoporous Prussian blue nanoparticles loading doxorubicin for fluorescence-guided tri-modal combination therapy of cancer, Nanoscale 11 (2019) 5717–5731, https://doi.org/10.1039/c8nr10430a.
[26] L. Jing, S. Shao, Y. Wang, Y. Yang, X. Yue, Z. Dai, Hyaluronic acid modified hollow Prussian blue nanoparticles loading 10-hydroxycamptothecin for targeting thermochemotherapy of cancer, Theranostics 6 (2016) 40–53, https://doi.org/10.7150/thno.13250.
[27] W. Wu, L. Yu, Y. Pu, H. Yao, Y. Chen, J. Shi, Copper-enriched Prussian blue nanomedicine for in situ disulfiram toxification and photothermal antitumor amplification, Adv. Mater. 32 (2020), e2000542, https://doi.org/10.1002/adma.202000542.
[28] B. Liu, W. Wang, J. Fan, Y. Long, F. Xiao, M. Daniyal, C. Tong, Q. Xie, Y. Jian, B. Lin, X. C Ma, W. Wang, RBC membrane camouflaged Prussian blue nanoparticles for gamabutolin loading and combined chemo/photothermal therapy of breast cancer, Biomaterials 217 (2019) 119301, https://doi.org/10.1016/j.biomaterials.2019.119301.
[29] S. Alona, C. Tsuf, C. Enav, M. Boaz, Near-infrared light induced phase transition of biodegradable composites for on-demand healing and drug release, ACS Appl. Mater. Interfaces 10 (2018) 4131–4139, https://doi.org/10.1021/acsami.7b17481.
[30] L. Tong, Y. Zhao, T.B. Huff, M.N. Hansen, A. Wei, J. Cheng, Gold nanorods mediate tumor cell death by compromising membrane integrity, Adv. Mater. 19 (2007) 3136–3141, https://doi.org/10.1002/adma.200701974.
[31] V. Oakes, W. Wang, B. Harrington, W.J. Lee, H. Beamish, K.M. Chia, A. Pinder, H. Goto, M. Inagaki, S. Pavey, B. Gabrielli, CyclinA/Cdk2 regulates Cdh1 and claspin during late S/G2 phase of the cell cycle, Cell Cycle 20 (2014) 3302–3311, https://doi.org/10.4161/15384101.2014.949111.
[32] E. Lees, B. Faha, V. Dulic, S.I. Reed, E. Harlow, Cyclin E/cdk2 and cyclin A/cdk2 kinases associate with p107 and E2F in a temporally distinct manner, Genes Dev. 10 (1992) 1847–1885, https://doi.org/10.1101/gad.6.10.1874.
[33] S. Revathidevi, A.K. Munirajan, Akt in cancer: mediator and more, Semin. Canc. Biol. 59 (2019) 80–91, https://doi.org/10.1016/j.semcancer.2019.06.002.
[34] M. Song, A.M. Bode, Z. Dong, M. Lee, Akt as a therapeutic target for cancer, Canc. Res. 79 (2019) 1019–1031, https://doi.org/10.1158/0008-5472.CAN-18-2738.
[35] J.A. Bertout, S.A. Patel, M.C. Simon, The impact of O_2 availability on human cancer, Nat. Rev. Canc. 8 (2008) 967–975, https://doi.org/10.1038/nrc2540.
[36] J.E. Ziello, I.S. Jovin, Y. Huang, Hypoxia-inducible factor (HIF)-1 regulatory pathway and its potential for therapeutic intervention in malignancy and ischemia, Yale J. Biol. Med. 80 (2007) 51–60. https://pubmed.ncbi.nlm.nih.gov/18160990/.
[37] S.J. Dixon, K.M. Lemberg, M.R. Lamprecht, R. Skouta, E.M. Zaitsev, C.E. Gleason, D.N. Patel, A.J. Bauer, A.M. Cantley, W.S. Yang, B. Morrison, B.R. Stockwell, Ferroptosis: an iron-dependent form of nonapoptotic cell death, Cell 149 (2012) 1060–1072, https://doi.org/10.1016/j.cell.2012.03.042.
[38] X. Chen, R. Kang, G. Kroemer, D. Tang, Broadening horizons: the role of ferroptosis in cancer, Nat. Rev. Clin. Oncol. 18 (2021) 280–296, https://doi.org/10.1038/s41571-020-00462-0.
[39] J.G. Kim, S.C. Lee, O. Kim, K. Kim, K.Y. Song, S.K. Lee, B.J. Choi, W. Jeong, S. Kim, HSP90 inhibitor 17-DMAG exerts anticancer effects against gastric cancer cells principally by altering oxidant-antioxidant balance, Oncotarget 8 (2017) 56473–56489, https://doi.org/10.18632/oncotarget.17007.
[40] J. Shi, Z. Xiao, N. Kamaly, O.C. Farokhzad, Self-assembled targeted nanoparticles: evolution of technologies and bench to bedside translation, Acc. Chem. Res. 44 (2011) 1123–1134, https://doi.org/10.1021/ar200054n.

[41] H. Koo, M.S. Huh, I. Sun, S.H. Yuk, K. Choi, K. Kim, I.C. Kwon, In vivo targeted delivery of nanoparticles for theranosis, Acc. Chem. Res. 44 (2011) 1018–1028, https://doi.org/10.1021/ar2000138.
[42] G. Wen, X. Li, Y. Zhang, X. Han, X. Xu, C. Liu, K. Chan, C. Lee, C. Yin, L. Bian, L. Wang, Effective phototheranostics of brain tumor assisted by near-infrared-II light-responsive semiconducting polymer nanoparticles, ACS Appl. Mater. Interfaces 12 (2020) 33492–33499, https://doi.org/10.1021/acsami.0c08562.
[43] C. Yin, X. Li, G. Wen, B. Yang, Y. Zhang, X. Chen, P. Zhao, S. Li, R. Li, L. Wang, C. Lee, L. Bian, Organic semiconducting polymer amphiphile for near-infrared-II light-triggered phototheranostics, Biomaterials 232 (2020) 119684, https://doi.org/10.1016/j.biomaterials.2019.119684.
[44] N. Fan, F. Cheng, J.A. Ho, C. Yeh, Photocontrolled targeted drug delivery: photocaged biologically active folic acid as a light-responsive tumor-targeting molecule, Angew Chem. Int. Ed. Engl. 51 (2012) 8806–8810, https://doi.org/10.1002/anie.201203339.
[45] H. Cho, H.Y. Yoon, H. Koo, S. Ko, J. Shim, J. Lee, K. Kim, I.C. Kwon, D. Kim, Self-assembled nanoparticles based on hyaluronic acid-ceramide (HA-CE) and Pluronic® for tumor-targeted delivery of docetaxel, Biomaterials 32 (2011) 7181–7190, https://doi.org/10.1016/j.biomaterials.2011.06.028.
[46] M. Alas, A. Saghaeidehkordi, K. Kaur, Peptide-drug conjugates with different linkers for cancer therapy, J. Med. Chem. 64 (2021) 216–232, https://doi.org/10.1021/acs.jmedchem.0c01530.
[47] X. Qu, P. Qiu, Y. Zhu, M. Yang, C. Mao, Guiding nanomaterials to tumors for breast cancer precision medicine: from tumor-targeting small-molecule discovery to targeted nanodrug delivery, NPG Asia Mater. 9 (2017) e452, https://doi.org/10.1038/am.2017.196.